ADVANCED FUNCTIONAL MATERIALS
www.afm-journal.de

Extreme Two-Phase Cooling from Laser-Etched Diamond and Conformal, Template-Fabricated Microporous Copper

*James W. Palko, Hyoungsoon Lee, Chi Zhang, Tom J. Dusseault, Tanmoy Maitra, Yoonjin Won, Damena D. Agonafer, Jess Moss, Farzad Houshmand, Guoguang Rong, Joshua D. Wilbur, Derrick Rockosi, Ihor Mykyta, Dan Resler, David Altman, Mehdi Asheghi, Juan G. Santiago, and Kenneth E. Goodson**

This paper reports the first integration of laser-etched polycrystalline diamond microchannels with template-fabricated microporous copper for extreme convective boiling in a composite heat sink for power electronics and energy conversion. Diamond offers the highest thermal conductivity near room temperature, and enables aggressive heat spreading along triangular channel walls with 1:1 aspect ratio. Conformally coated porous copper with thickness 25 μm and 5 μm pore size optimizes fluid and heat transport for convective boiling within the diamond channels. Data reported here include 1280 W cm^{-2} of heat removal from 0.7 cm^2 surface area with temperature rise beyond fluid saturation less than 21 K, corresponding to 6.3×10^5 W m^{-2} K^{-1}. This heat sink has the potential to dissipate much larger localized heat loads with small temperature nonuniformity (5 kW cm^{-2} over 200 μm × 200 μm with <3 K temperature difference). A microfluidic manifold assures uniform distribution of liquid over the heat sink surface with negligible pumping power requirements (e.g., $<1.4 \times 10^{-4}$ of the thermal power dissipated). This breakthrough integration of functional materials and the resulting experimental data set a very high bar for microfluidic heat removal.

1. Introduction

The removal of extreme heat fluxes is a very important problem for electronics in applications including high frequency radar,[1] renewable power generation and electric vehicles,[2] and high performance computing.[3] These applications feature chip-average heat fluxes exceeding 1 kW cm^{-2} and much higher fluxes at localized hotspots and are often thermally limited, i.e., their design and performance could be improved if better cooling technologies were available.[1] Two-phase liquid/vapor cooling is attractive for these applications based on the high heat fluxes and low superheats achievable.[4] Two-phase cooling systems can take a variety of forms including pool boiling,[5] flow boiling,[6–9] jet impingement/spray,[10] and evaporation or boiling in porous media.[11,12] Design of the materials used to enable two-phase cooling and their integration into systems is key to achieving advances in thermal management.

In particular, boiling in porous materials formed into films thinner than about 35 μm with small pore size (e.g., 5 μm) can facilitate exceptionally high heat transfer coefficients, h, exceeding 10^6 W m^{-2} K^{-1}.[13] The key characteristics of these films are high thermal conductivity of the matrix material, uniformity of pore dimensions, and small pore size. High thermal conductivity reduces thermal resistance for distribution of heat through the porous matrix itself. A large number of porous

Dr. J. W. Palko, C. Zhang, T. J. Dusseault, Dr. T. Maitra, J. Moss, Dr. F. Houshmand, J. D. Wilbur, Prof. M. Asheghi, Prof. J. G. Santiago, Prof. K. E. Goodson
Department of Mechanical Engineering
Stanford University
Stanford, CA 94305, USA
E-mail: goodson@stanford.edu
Prof. J. W. Palko
Department of Mechanical Engineering
University of California
Merced, Merced, CA 06974, USA
Prof. H. Lee
School of Mechanical Engineering
Chung-Ang University
Seoul 06974, South Korea
Prof. Y. Won
Department of Mechanical and Aerospace Engineering
University of California
Irvine, Irvine, CA 92697, USA
Prof. D. D. Agonafer
Department of Mechanical Engineering and Materials Science
Washington University
St. Louis, MO 63130, USA
Prof. G. Rong
Electronics and Communication Engineering Department
Suzhou Vocational Institute of Industrial Technology
Suzhou 215021, China
D. Rockosi, I. Mykyta, D. Resler, D. Altman
Advanced Technology Programs
Raytheon Integrated Defense Systems
Sudbury, MA 01776, USA

DOI: 10.1002/adfm.201703265

wicks have demonstrated the capability of dissipating significant heat fluxes in boiling.[11,14–17] However, materials with carefully controlled microstructures having uniform, fine pore sizes show particularly high heat transfer coefficients.[13,18] Small pore dimensions increase internal surface area. Narrow distributions of pore sizes promote uniform bubble generation during boiling and improve consistency of capillary forces, which may promote stable films of minimized thickness. Such a porous material must, additionally, be deposited in thin layers that minimize total conductive transport and vapor escape distances. Copper electrodeposited around a sacrificial template provides the necessary microstructural control and thermal conductivity as well as intimate substrate contact.[19,20]

Despite the remarkable heat transfer coefficients provided by boiling in porous films, fluid transport constraints can limit the heat fluxes, which can be treated over areas relevant for most applications (e.g., >1 cm^2). Rewetting of the porous film by capillary action has been shown to play a key role in determining the maximum heat flux that can be dissipated or "critical heat flux" (CHF).[21] Dhillon et al. showed the existence of maxima in CHF with porous feature spacing resulting from the competition of viscous resistance to liquid rewetting and capillary and bulk pressure driven flows.[22] Structures that define paths for liquid delivery and potentially reduce the required rewetting distance can enhance boiling performance.[23]

To further extend surface-normalized convective performance, heat sinks typically use extended surfaces. However, to apply this approach with the high h values achievable by boiling in thin porous films, a very high thermal conductivity, k, for the material forming the extended surfaces is required to maintain acceptable efficiency of the surfaces. The fin efficiency quantifies the uniformity of temperature along the fins and improves with the thermal conductivity and thickness of the fin material.[24] As an example, even a low aspect ratio fin of triangular cross-section and equal height and base width of 500 µm formed from silicon gives <40% efficiency with surface $h = 10^6$ W m^{-2} K^{-1} due to the thermal resistance for conduction through the fin (see Figure S1, Supporting Information). Management of extreme heat fluxes via boiling on structured surfaces is therefore a complex materials design and integration problem balancing the local enhancement of the surface and transport within the structure.

2. Results and Discussion

2.1. Integration of Template-Fabricated Porous Copper with Diamond Extended Surfaces

Here, we address the limitations of boiling in porous media using diamond to create effective extended surfaces along with microfluidic liquid supply for use with the high heat transfer coefficients provided. High quality chemical vapor deposited (CVD) diamond, as used here, is now readily available with room temperature conductivities[25] exceeding 1800 W m^{-1} K^{-1} and has proved very effective as a heat spreader in a variety of thermal applications.[26,27] A triangular fin with height and base of 500 µm formed from CVD diamond (k = 1800 W m^{-1} K^{-1}) provides an efficiency of ≈89% (see Figure S1, Supporting Information) with the high h values achievable via boiling in a fine porous surface layer ($h = 10^6$ W m^{-2} K^{-1}).

Figure 1a shows cross-sectional scanning electron images (SEM) of a two-phase heat sink created by integration of thin (25 µm) electrodeposited porous copper layers (see right image showing focused ion beam cutout) and laser micromachined diamond. Figure 1b is a schematic of the heat sink in operation. Heat applied to the base of the heat sink is spread by the

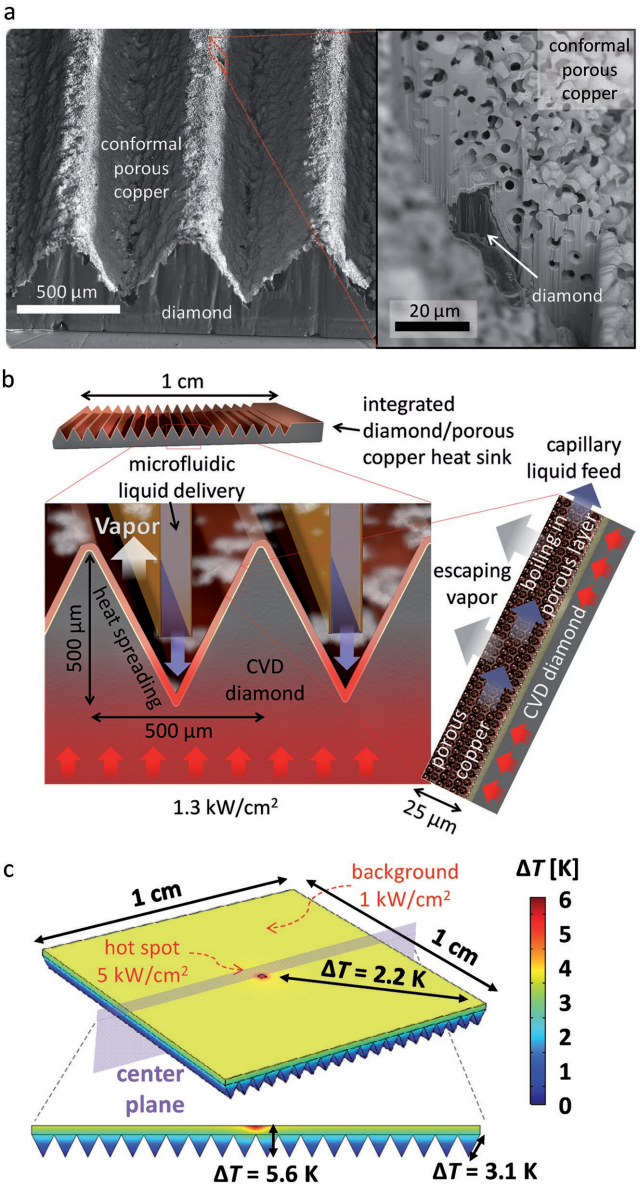

Figure 1. Laser micromachined diamond heat spreaders with integrated conformal porous copper. a) Backscatter SEM images of integrated heat spreader with triangular fins having height and base width both equal to 500 µm. Right image shows a focused ion beam cross-section of the porous copper layer indicating its ability to conform to substrate roughness. b) Schematic of heat sink operation. Liquid is supplied to the bottom of micromachined channels in the diamond heat spreader, where it wicks into the conformal porous copper layer and boils to vapor. c) Simulated temperature for heat spreader in operation with surface $h = 10^6$ W m^{-2} K^{-1}.

diamond, reducing the heat flux at the extended surfaces where it is removed to the working fluid. Liquid coolant is supplied at the base of each extended surface by a microfluidic manifold[28] (see Figures S4–S7, Supporting Information) and is wicked throughout the porous structure under capillary action.

The scale at which extended surfaces implemented in the heat spreader can remain useful is set by liquid transport limitations. The fine feature size of the porous material, which enables an exceptionally high heat transfer coefficient, also severely limits the lengths over which such porous structures can be effective when operating via capillary action.[13] The capillary driving pressure for liquid transport within a porous material scales with the inverse of pore diameter, but the permeability scales as the square of pore diameter, so that the net result is a decrease in capillary transport with decreasing feature size (neglecting other effects such as gravity).[29] To overcome this limitation, we implement small scale extended surfaces with liquid transport lengths on the order of 500 µm based on the demonstrated performance of the porous copper material at similar scales.[13]

In addition to facilitating efficient extended surfaces, the high thermal conductivity of diamond effectively spreads lateral inhomogeneities in heating, which is an essential function for many electronics applications.[30,31] Figure 1c shows a finite element simulation of the surface temperature for the heat sink under example operating conditions. The heat spreader has a 1 cm × 1 cm heated area with a 200 µm × 200 µm localized hot spot at the center of the device. Triangular channels have a depth of 500 µm and a spacing of 500 µm. The total thickness of the heat spreader is 700 µm and the thermal conductivity of the diamond is set to $k = 1800$ W m^{-1} K^{-1}. 1 kW cm^{-2} heat flux is applied over the entire heated area with 5 kW cm^{-2} heat flux at the hot spot. A constant heat transfer coefficient of $h = 10^6$ W m^{-2} K^{-1} is applied on the extended surfaces based on measurements of boiling heat transfer in porous copper at small scales.[13] Temperature difference from the hotspot to the heat sink surface under these conditions is less than 6 K, while temperature difference across the heated area is 2.2 K, and that from fin base to tip is 3.1 K. For comparison, silicon ($k = 150$ W m^{-1} K^{-1}) gives a maximum temperature difference exceeding 50 K under identical conditions.

2.2. Diamond Heat Sink Fabrication

Given the high thermal conductivity and heat transfer coefficients provided by the diamond and porous copper materials, respectively, the challenge is to integrate these materials in the final required geometry. **Figure 2** shows the fabrication process for the integrated heat sink, with each step of the process described below and detailed in the Experimental Section.

We form the extended surfaces in CVD diamond dies (1 cm × 1 cm × 700 µm) using laser (1064 nm Nd:YAG) micromachining (Figure 2a).[32] High aspect ratio extended surfaces are achievable with the laser machining process, but we target a 1:1 ratio for the base to height of the triangular fins to maintain high efficiency of the surfaces.

The laser ablation process can form surface deposits of graphitic carbon.[33] This residue presents two difficulties: It prevents adequate adhesion of metallic layers used in the integration of the porous material, and it degrades thermal

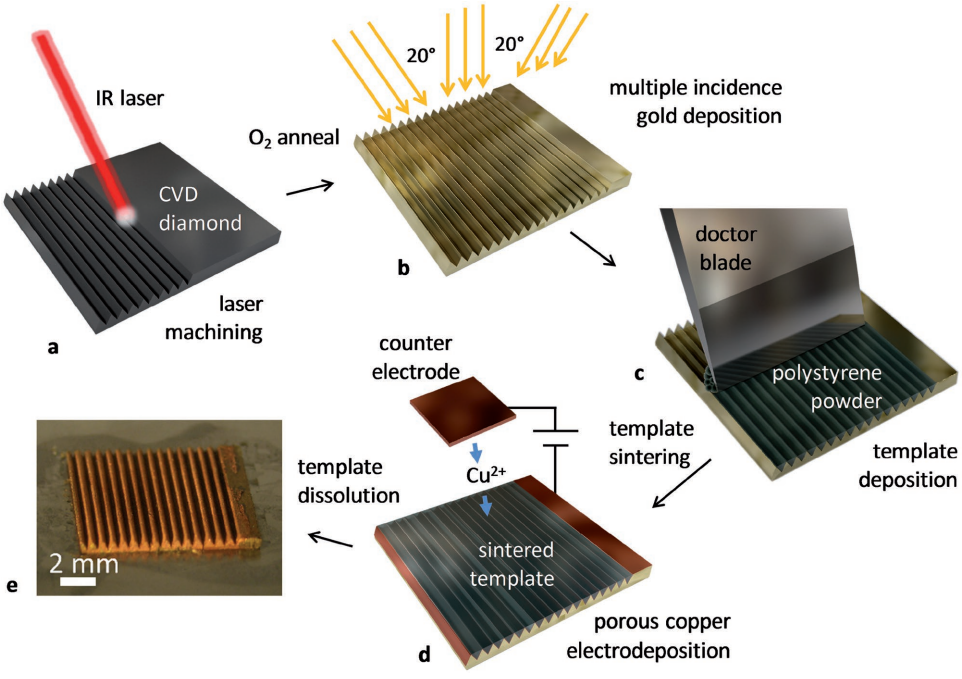

Figure 2. Schematic of integration process. a) IR laser micromachining of CVD diamond die followed by annealing in oxygen atmosphere for graphitic carbon removal. b) Evaporation of gold (with titanium adhesion layers) from three separate incidence angles to form conformal gold working electrode for electrodeposition. c) Doctor blade deposition of polystyrene powder template defining inverse structure of porous copper followed by heating to optimize permeability. d) Electrodeposition of porous copper structure around template. e) Optical image of integrated porous copper/diamond heat sink following dissolution of polymer template with solvent.

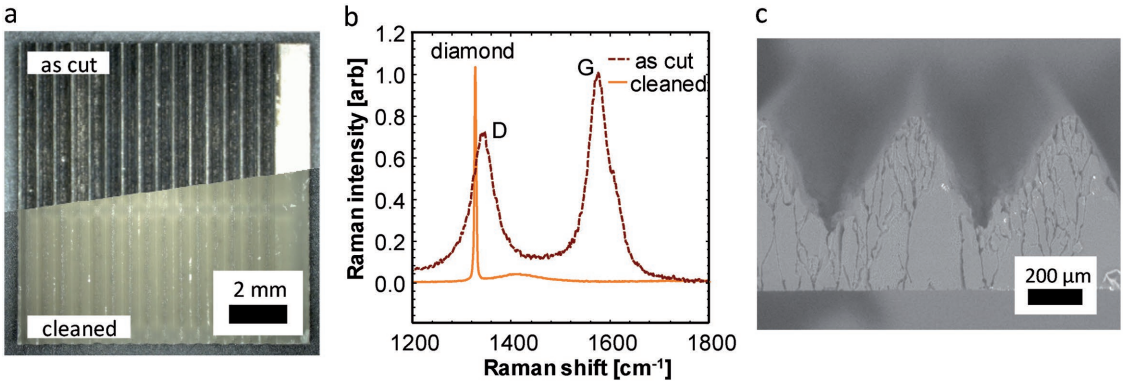

Figure 3. Cleaning of residual graphitic carbon. a) Combination image of CVD diamond die following laser micromachining and residual carbon removal. b) Normalized Raman spectra of die following cutting (red) and after annealing at 500 °C for 12 h in an oxygen atmosphere (yellow). c) Grain boundary etching due to high-temperature oxygen annealing.

performance due to its reduced thermal conductivity. We, therefore, remove this graphitic residue using oxidation in an O_2 atmosphere at elevated temperature. **Figure 3**a is a combination image showing the effect of residual carbon removal following cutting (in this case using an inductively coupled oxygen plasma).

Micro-Raman spectroscopy reveals details about the bonding for carbon near the surface of the dies following processing. Figure 3b shows micro-Raman spectra for a diamond die following cutting and cleaning. Spectra collected following cutting show a clear graphitic (sp^2) carbon peak (G peak) near 1575 cm^{-1} as well a prominent disorder peak (D peak) centered near 1340 cm^{-1} associated with small grain sizes in these systems.[34] Cleaning in an oxygen atmosphere at 500 °C for 12 h recovers the sharp emission peak at 1330 cm^{-1} associated with high quality diamond. High-temperature oxygen atmosphere annealing however, also produces significant grain boundary etching (Figure 3c). This effect adds to the existing roughness of the diamond surface resulting from the laser machining process, but does not appreciably affect function due to the conformal nature of the porous coating.

We characterized the surface roughness resulting from laser ablation and graphitic carbon removal. Root mean square (RMS) roughness values of 3.4 µm were found for a representative channel side wall. Detailed roughness profiles are given in the Supporting Information.

Once the diamond substrate is formed to the desired geometry and cleaned to provide the necessary surface state, we deposit a layer of fine featured porous copper conformally on its surface. The porous layer is produced by electrodeposition around a sacrificial template that defines the inverse structure. This method has been applied before for a variety of applications.[35–38]

A thin conductive layer deposited on the diamond substrate acts as a working electrode during electrodeposition (Figure 2b). Gold is chosen as the primary constituent of the electrode layer based on its corrosion resistance in acidic electroplating solutions. The working electrode is deposited via electron beam evaporation as a sequence of three bilayers each consisting of 15 nm of Ti followed by 100 nm of Au. To provide continuity over the rough surface produced by laser cutting and residual carbon removal operations we apply each evaporation with a different incidence angle (normal to the heat spreader plane and with rotations of ±20° about the channel axes). The Ti layer provides excellent bonding to diamond substrates, which may otherwise show poor adhesion, with adhesion strengths exceeding 80 MPa for brazed Ti/diamond interfaces.[39] We also note that heat sinks, as fabricated, survive repeated temperature cycling with temperature swings well in excess of 100 °C. Despite the large disparity in thermal expansion coefficient for diamond (1.79×10^{-6} K^{-1} at 400 K)[40] and copper (17.5×10^{-6} K^{-1} at 400 K),[41] we observed no delamination, indicating the robustness of the copper/diamond bond provided by the Ti/Au seed layer.

The template defining the inverse of the final porous structure consists of spherical polystyrene particles produced by dispersion polymerization.[42] These particles are highly monodisperse with a median diameter of 5 µm. The electrodeposition technique decouples the deposition of template from growth of the porous material, and the thickness of the final porous layer is defined by the electrodeposition parameters, not the template. The channels in the heat sink surface are completely filled with template material, using doctor blading with a dry powder of template spheres.

As deposited, the template consists of a bed of randomly packed spheres. The inverse of this structure shows minimal permeability due to the small contact area between the spheres, which translate to small necks between the pores. Sintering of the template (103 °C, 90 min.) increases the contact area between spheres and consequently the neck size between pores, enhancing permeability. Porous copper layers produced using this protocol show permeabilities of 4.5×10^{-13} m^2.[43]

Following template deposition and modification, we electrodeposit copper from a sulfate based electroplating bath throughout the interstices of the template. Porous copper is deposited to a mean thickness of 25 µm. Electrodeposition bath chemistry and deposition parameters are described in the Experimental Section. After electrodeposition, the structure consists of a solid composite of polymer template and electrodeposited copper. We dissolve the polymer template using tetrahydrafuran solvent overnight at room temperature revealing the final porous copper structure (Figure 1a). As

shown in Figure 1a, the CIO is able to conform to both the large and small-scale topography of the diamond heat sink. The electrodeposition process fills in small-scale features at the diamond surface. We measured the roughness of CIO grown on a planar silicon substrate to be 0.6 µm (RMS). Detailed profiles for the CIO surface are provided in the Supporting Information. Figure 2e shows an image of a complete integrated diamond/porous copper heat spreader.

2.3. Heat Transfer Performance

We evaluated the heat transfer performance of the integrated heat spreader in boiling (Figure 1b). Liquid water at room temperature was supplied to the base of the heat sink channels using a microfluidic manifold (see Figures S4–S7, Supporting Information).[28] Vapor was allowed to vent to ambient. Design of the heat transfer experimental setup including the geometry and construction of the manifold are detailed in the Supporting Information. The heat sink received heat through a silicon substrate with a thin film platinum heater deposited on the opposite side, with temperature at the heater surface measured by a thermocouple. The heated area was 7 mm × 10 mm. Due to the high heat fluxes required, the thermal interface between the silicon substrate and diamond is key to conducting and interpreting heat transfer experiments in this configuration. The exceptionally low thermal expansion of diamond (1.79×10^{-6} K^{-1} at 400 K) compared to silicon (3.15×10^{-6} K^{-1} at 400 K) also creates interface reliability challenges over the relatively large heated area.[40] Liquid eutectic GaInSn served as a thermal interface material (TIM) for mating the silicon and the diamond. This TIM has a relatively high thermal conductivity, $k = 27.6$ W m^{-1} K^{-1},[44] with excellent accommodation of differential expansion and roughness of the diamond surface.

Figure 4 shows heat flux at the heated surface, q'', as a function of diamond base temperature, T_{base}, (calculated from the heater centerline temperature) using water as the working fluid with liquid flow rates of $Q = 3.1$ and 1.0 mL s^{-1}. The integration of diamond and finely porous materials facilitates dissipation of more than 1300 W cm^{-2} at temperatures less than 35 K above saturation (i.e., 135 °C). Also shown in Figure 4 for comparison are data from Chu et al.[45] for a micro/nanotextured copper oxide surface, representative of state of the art pool boiling systems with porous enhancement, capable of dissipating around 250 W cm^{-2}.

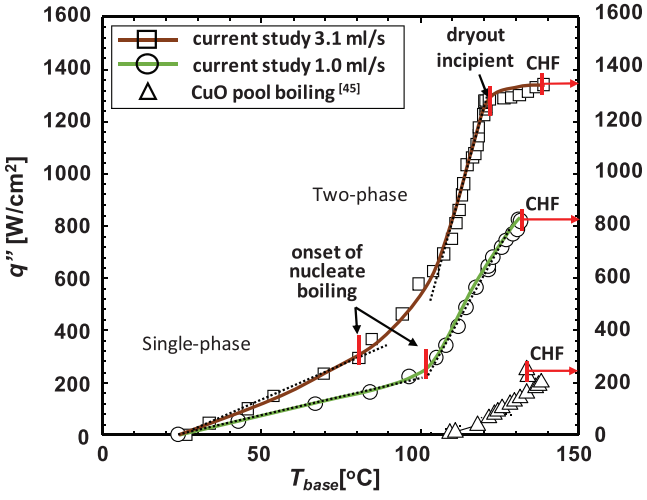

Figure 4. Boiling heat transfer performance for integrated diamond/porous copper heat sink using water working fluid at volumetric flow rates of 3.1 mL s^{-1} (squares) and 1.0 mL s^{-1} (circles) with 0.7 cm^2 heated area. Heat flux at heater surface is plotted versus heat sink base temperature calculated from heater surface temperature. Data from Chu et al.[45] for pool boiling from a nano/microtextured geometry are shown for comparison.

The force feeding of subcooled liquid to the diamond/porous copper heat sink surface provides a significant single-phase contribution to the cooling. The configuration of the manifold is similar to a slot jet impingement geometry, but the velocities considered here are much lower than commonly applied in jet impingement.[46] The single-phase heat transfer coefficients for the system corresponding to the heat flux at the heater, q'', are $(5.4 \pm 0.2) \times 10^4$ W m^{-2} K^{-1} and $(3.0 \pm 0.3) \times 10^4$ W m^{-2} K^{-1} for flow rates of 3.1 and 1.0 mL s^{-1}, respectively. These are comparable to those found for single-phase convection in microchannels but at substantially lower Reynolds numbers.[4] Up to heat fluxes of ≈220 W cm^{-2} (and temperatures of ≈95 °C) in the low flowrate case and ≈300 W cm^{-2} (and ≈80 °C) in the high flowrate case, q'' and T_{base} show a linear relationship corresponding to single-phase convection.

At higher heat fluxes, a change in heat transfer coefficient indicates the onset of nucleate boiling.[47,48] The change is abrupt for $Q = 1.0$ mL s^{-1}, but more gradual for $Q = 3.1$ mL s^{-1}. This gradual change may be related to inhomogeneous flow and nonuniform onset of boiling. Above 750 W cm^{-2} and 110 °C the q'' versus T_{base} curve is again linear for high flow rate, indicating a complete transition to boiling. Following transition to boiling, the mean heat transfer coefficient for the system, (referenced to fluid saturation temperature, 100 °C), is $(6.5 \pm 0.3) \times 10^5$ W m^{-2} K^{-1} for 750 W cm^{-2} ≤ q'' ≤ 1250 W cm^{-2} and $Q = 3.1$ mL s^{-1} and $(2.8 \pm 0.1) \times 10^5$ W m^{-2} K^{-1} for 400 W cm^{-2} ≤ q'' ≤ 820 W cm^{-2} and $Q = 1.0$ mL s^{-1}. We hypothesize that the dependence on flow rate is a further result of inhomogeneities in flow. Flow maldistribution leads to dryout in regions of the porous layer, and these regions grow at higher heat fluxes and low flow rates.

Sufficient further increase in heat flux results in an abrupt increase in temperature (i.e., "burnout") corresponding to the critical heat flux. In this study, CHF occurred at 820 W cm^{-2} for 1.0 mL s^{-1} and 1340 W cm^{-2} for 3.1 mL s^{-1}. The onset of CHF was abrupt at low flow rate, but more gradual for higher flow rate, with initial decrease in heat transfer coefficient beginning at ≈1280 W cm^{-2} and ≈120 °C. CHF is not the result of global liquid starvation, as only a fraction of the liquid supplied is vaporized. At CHF, 27% of liquid supplied is vaporized for 1.0 mL s^{-1} flowrate, while 14% is vaporized at $Q = 3.1$ mL s^{-1}, based on energy balance assuming no superheating of the escaping vapor and subtracting single-phase contributions. The experimental facility does not allow visualization of the phenomena leading to burnout due to the required configuration of the manifold, but based on similar systems (e.g., pool boiling, jet impingement) we expect the CHF to correspond to a condition where vapor flow resistance retards escape and leads to vapor blanketing of the porous layer.[5] More uniform liquid supply at higher flow rate likely minimizes the transport

distances over which capillary suction must act in the porous layer to replenish liquid films, thus leading to increased CHF at these flowrates. Higher flowrates also may provide additional vapor clearance by entrainment. Jet impingement directly beneath the liquid delivery channels of the manifold may act to prevent dryout in this immediate area, and account for the more gradual signature of burnout seen for 3.1 mL s^{-1} flowrate. However, we note that the available flow rate does not represent the ultimate limit to heat flux. Flow rates above 3 mL s^{-1} were tested and were not found to increase the CHF significantly, indicating that the primary mechanism controlling CHF at these flow rates is intrinsic to the porous film. The maximum surface heat flux seen at the initiation of burnout, (580 W cm^{-2} = 1280 W cm^{-2} base heat flux/ 2.2 surface to base area enhancement) corresponds relatively closely to that measured over small areas (0.6 mm^2) for similar thickness (25 µm) films on planar substrates (700 W cm^{-2}).[13] We hypothesize that vapor clearance or capillary transport limitations may control the ultimate heat flux that the system can manage.

The pressure drops from liquid inlet to ambient for the 3.1 and 1.0 mL s^{-1} flowrates, were 42 and 16 kPa, respectively. The ratios of dissipated heat at CHF to power required to pump the coolant (coefficient of performance) for the high and low flowrates are >7000 and >37 000, respectively. Hence, the power required for the cooling solution is negligible compared to the dissipated heat.

Temperature was measured at the center of the heated surface. Given the large lateral extent of the heater compared to the silicon substrate thickness (≈13×) and high heat transfer coefficient provided by the diamond heat spreader, the heat flux near the center of the heater is expected to be transmitted directly to the heat spreader without significant reduction (see Figure S9, Supporting Information). Determination of temperature at the bottom of the diamond heat spreader requires correction for temperature drop due to conduction from the heater surface through the silicon to the diamond. Figure 4 shows calculated temperature at the diamond base accounting for conduction through the silicon substrate (including temperature dependence of its thermal conductivity)[49] for an assumed negligible TIM thickness.

3. Conclusion

The integration of CVD diamond and porous copper materials with finely tuned microstructure provides the capability to remove very high heat fluxes from large areas and spread heat from exceptionally intense hot spots. The continuing improvement of conductivity for synthetic diamond materials provides the opportunity to push this performance further, especially in combination with readily achievable decreases in the feature size of engineered porous metals, which can lead to still higher heat transfer coefficients. The penalty for this modification is lower permeability, potentially requiring smaller extended surface features and more precise microfluidic manifolding. The necessary precision to define these features is available with laser ablation for diamond and a variety of microfabrication and additive manufacturing techniques for relevant manifold designs and materials. Alternatively, phase separation approaches have shown promise for driving liquid supply for boiling and evaporation with pressures in excess of that available by capillary action alone offering potential to overcome permeability limitations.[28,50] The integration of high conductivity materials and engineered microstructure materials thus provides an avenue for pushing the capabilities of two-phase cooling to its physical limits.

4. Experimental Section

Diamond Laser Ablation and Characterization: The diamond heat spreaders were laser micromachined using a 1064 nm Nd:YAG laser from CVD grown diamond dies (TM200, Element Six) with thickness of 700 µm. Oxygen gas was flowed over the die during ablation, and the die was affixed to a stage maintained at 0 °C. Graphitic carbon was removed from the diamond surface following ablation by exposure to an oxygen atmosphere at 500 °C for 12 h. The surface of the diamond was characterized using micro-Raman spectroscopy.[51] The sample was illuminated with a 532 nm laser with a power of 3 mW through a 100× objective providing a spot size less than 1 µm.

Templated Porous Copper Synthesis: Porous copper was deposited conformally on the diamond heat spreader using electrodeposition around a sacrificial template.[20,38] Three metal bilayers, each consisting of a titanium adhesion layer (15 nm) and a gold seed layer (100 nm), were evaporated on the diamond heat spreader. The Ti/Au seed layers serve as the cathode for the copper electrodeposition. The bilayers were deposited with three separate angles of incidence, normal to the heat spreader base and with rotations of ±20° around the channel axes, resulting in adequate coating of the rough diamond surfaces produced by laser ablation with electrical continuity over the entire surface.

Polystyrene microspheres with mean diameter of 5 µm were synthesized using emulsion polymerization.[42] Templates consisting of dry polystyrene microspheres were packed in trenches of the heat spreader with a doctor blade resting on the tops of the heat spreader ridges and moved in the direction of the channels axes. The packed polystyrene beds were sintered at 103° ± 0.5 °C for 90 min in a conventional oven for microstructure refinement.

In preparation for electrodeposition, the template bed was first wetted with ethanol before immersion of the heat spreader into the plating solution to aid infiltration. Copper was electrodeposited from aqueous solution (0.6 M $CuSO_4$ + 5 × 10^{-3} M H_2SO_4) with potentiostatic electrodeposition at a constant overpotential of 80 mV for 4.5 h. Following electrodeposition, the polystyrene template was dissolved by immersion in tetrhydrofuran overnight.

Thermal Characterization: The diamond heat spreader was heated by a thin-film Pt resistance heater, deposited on an Si wafer (525 µm thickness). A thin film of GaInStan (eutectic Ga-In-Sn) liquid metal alloy was used as a thermal interfacial material between the Si wafer and the diamond heat spreader to minimize contact resistance and absorb thermal expansion mismatch between diamond and Si.

Filtered deionized water was supplied to the heat spreader via the manifold by a calibrated magnetically driven gear pump. Prefiltered deionized water was used as the working fluid without recycling in all experiments. An inline flow regulator was used to compensate for any flow instabilities during the experiment.

Heater temperature was measured by a type-K thermocouple attached to the center of the heated area and electrically isolated from the heater by a thin (50 µm) polyimide layer. Temperature at the base of the heat sink was determined based on integration of the temperature drop through the silicon wafer using the temperature dependent conductivity of silicon.[49] Liquid inlet temperature was measured by a type-K thermocouples upstream of the test module, and pressure was measured at the inlet of the test module using a Bourdon tube pressure gauge.

Water flow rate was gradually increased up to the desired values. Once the flow stabilized at the desired operating conditions, the

electrical power to the thin-film Pt heater in the test module was increased in small increments until the critical heat flux was observed.

Measurement Error and Uncertainty Analysis: The main uncertainties in measurement of the heat transfer performance are caused by (1) heat losses to the ambient, (2) uncertainties in measurement of the total power input, and (3) uncertainties in determination of the heater temperature and corresponding temperatures at the diamond heat spreader base. These are each considered below.

Dominant heat losses to the ambient occur at the bottom side of the heater. The heater is covered by a silicone insulator ≈6.4 mm thick to minimize heat loss during experiments. Since the thermal conductivity of the silicone insulator is only ≈0.2 W m^{-1} K^{-1}, the thermal resistance to the ambient due to the heat loss, R_{Loss}, is large compared to the extremely small equivalent thermal resistance on the active (boiling) side, $R_{Boiling}$. At CHF for the high flow rate case, R_{Loss} is 454 K W^{-1} while $R_{Boiling}$ is only 0.1 K W^{-1}. The difference between these thermal resistances is due to the large heat transfer coefficient of the boiling side compared to the small thermal conductivity of the silicone pad, resulting in small parasitic losses. Even neglecting thermal resistance for extraction of heat from the silicone (i.e., assuming silicone surface temperature equal to ambient), the heat loss to the ambient is only 0.03% of total power generated from the heater. Due to the relatively large heated area, parasitic heat loss was neglected through areas on the top surface of the heated silicon wafer that were adjacent to the heat sink.

Total power input was measured using a high resistance voltage divider (45 kΩ ± 0.1% + 5 kΩ ± 0.1%) for voltage measurement and a low resistance (0.05 Ω ± 1%) current sensing resistor. Voltage measurement uncertainty for the data acquisition system is ±0.02%. Propagating uncertainties using a small error approximation led to an overall uncertainty in power input of ≈1.2%.[52]

The type-K thermocouples used to measure heater and fluid temperatures have an uncertainty of ±0.5 K. The thickness tolerance of the silicon wafer is ±20 µm and corresponding uncertainty of the temperature drop though the Si substrate is up to ±1.7 K. Thickness of thermal interface material also affected temperature at the diamond heat spreader base. The liquid metal TIM used in this study made accurate thickness measurement difficult. Therefore, top Si substrate temperature is reported. To give an estimate for the bounds of the temperature difference between silicon and diamond, a maximum TIM thickness of 20 µm based on microscopic observation was estimated. At CHF for the high flow rate case (1340 W cm^{-2}), this yielded a difference in temperature between silicon and diamond of 9.7 K based on a TIM thermal conductivity of k = 27.6 W m^{-1} K^{-1}.[44]

Each data point represents 1 s corresponding to an average of 1000 samples from the data acquisition system. Heat transfer coefficients were calculated as slopes of linear regression fits for the range of heat fluxes stated. For single-phase values, intercepts were also fitted. For values corresponding to boiling, x-axis intercepts were fixed to saturation temperature (i.e., 100 °C). Stated error bounds for heat transfer coefficients correspond to 95% confidence intervals of the fitted values.[52]

Simulations: Simulations of conduction in the heat spreader were performed using the finite element method with COMSOL Multiphysics. Heat transfer in solids modules embedded in COMSOL was used for the calculation with maximum tolerance of 0.0001. The simulations used 1.1 million tetrahedral elements generated using a user-controlled mesh with an average mesh quality of 0.71. A constant heat transfer coefficient boundary condition with effective heat transfer coefficient of 1000 kW m^{-2} K^{-1} was applied at the diamond heat spreader fin surfaces and 100 °C was applied for the free stream external temperature.

Supporting Information

Supporting Information is available from the Wiley Online Library or from the author.

Acknowledgements

This project was supported in part by the U.S. Defense Advanced Research Projects Agency Microsystems Technology Office ICECool Fundamentals Program under Award No. HR0011-13-2-0011. The views, opinions, and/or findings contained in this article are those of the authors and should not be interpreted as representing the official views or policies, either expressed or implied of the Defense Advanced Research Projects Agency or Department of Defense. This work was partially supported by the U.S. National Science Foundation Engineering Research Center on Power Optimization of Electro-Thermal Systems (POETS) with cooperative agreement EEC-1449548. The authors thank Tanya Liu for assistance in figure preparation. Part of this work was performed at the Stanford Nano Shared Facilities (SNSF), supported by the National Science Foundation under Award No. ECCS-1542152.

Conflict of Interest

The authors declare no conflict of interest.

Keywords

boiling, diamond, laser ablation, porous copper, templated electrodeposition

Received: June 15, 2017
Revised: August 11, 2017
Published online:

[1] Y. Won, J. Cho, D. Agonafer, M. Asheghi, K. E. Goodson, *Proc. 2013 IEEE Compound Semiconductors Integrated Circuit Symp. (CSICS)*, IEEE, Piscataway, NJ **2013**, pp. 1–5.
[2] M. Andresen, M. Liserre, *Microelectron. Reliab.* **2014**, *54*, 1935.
[3] A. Bar-Cohen, K. J. L. Geisler, *Mech. Eng.* **2011**, *133*, 38.
[4] B. Agostini, M. Fabbri, J. E. Park, L. Wojtan, J. R. Thome, B. Michel, *Heat Transfer Eng.* **2007**, *28*, 258.
[5] I. Mudawar, *IEEE Trans. Compon. Packag. Technol.* **2001**, *24*, 122.
[6] S. G. Kandlikar, *Exp. Therm. Fluid Sci.* **2002**, *26*, 389.
[7] J. R. Thome, *Int. J. Heat Fluid Flow* **2004**, *25*, 128.
[8] P. A. Kottke, T. M. Yun, C. E. Green, Y. K. Joshi, A. G. Fedorov, *J. Heat Transfer* **2016**, *138*, 11501.
[9] R. K. Sarangi, A. Bhattacharya, R. S. Prasher, *Appl. Therm. Eng.* **2009**, *29*, 300.
[10] M. Visaria, I. Mudawar, *IEEE Trans. Compon. Packag. Technol.* **2009**, *32*, 784.
[11] J. A. Weibel, S. V. Garimella, *Adv. Heat Transfer* **2013**, *45*, 209.
[12] S. Li, R. Furberg, M. S. Toprak, B. Palm, M. Muhammed, *Adv. Funct. Mater.* **2008**, *18*, 2215.
[13] J. W. Palko, C. Zhang, J. D. Wilbur, T. J. Dusseault, M. Asheghi, K. E. Goodson, J. G. Santiago, *Appl. Phys. Lett.* **2015**, *107*, 253903.
[14] J. A. Weibel, S. V. Garimella, M. T. North, *Int. J. Heat Mass Transf.* **2010**, *53*, 4204.
[15] T. Semenic, I. Catton, *Int. J. Heat Mass Transfer* **2009**, *52*, 5113.
[16] Y. Nam, S. Sharratt, G. Cha, Y. S. Ju, *J. Heat Transfer* **2011**, *133*, 101502.
[17] J. L. Plawsky, A. G. Fedorov, S. V Garimella, H. B. Ma, S. C. Maroo, L. Chen, Y. Nam, *Nanoscale Microscale Thermophys. Eng.* **2014**, *18*, 251.
[18] D. Ćoso, V. Srinivasan, M.-C. Lu, J.-Y. Chang, A. Majumdar, *J. Heat Transfer* **2012**, *134*, 101501.
[19] M. T. Barako, J. M. Weisse, S. Roy, T. Kodama, T. J. Dusseault, M. Motoyama, M. Asheghi, F. B. Prinz, Z. Xiaolin, K. E. Goodson, *Proc. 2014 IEEE Intersociety Conf. on Thermal and Thermomechanical*

Phenomena in Electronic Systems (ITherm), IEEE, Piscataway, NJ **2014**, pp. 736–743.
[20] M. T. Barako, A. Sood, C. Zhang, J. Wang, T. Kodama, M. Asheghi, X. Zheng, P. V Braun, K. E. Goodson, *Nano Lett.* **2016**, *16*, 2754.
[21] M. Mccarthy, M. Rahman, E. Olceroglu, *Langmuir* **2014**, *30*, 11225.
[22] N. S. Dhillon, J. Buongiorno, K. K. Varanasi, *Nat. Commun.* **2015**, *6*, 8247.
[23] S. Mori, S. Mt Aznam, K. Okuyama, *Int. J. Heat Mass Transfer* **2015**, *80*, 1.
[24] A. D. Kraus, A. Aziz, J. Welty, *Extended Surface Heat Transfer*, John Wiley & Sons, Inc., New York **2001**, pp. 1–58.
[25] S. Coe, R. Sussmann, *Diam. Relat. Mater.* **2000**, *9*, 1726.
[26] G. D. Via, J. G. Felbinger, J. Blevins, K. Chabak, G. Jessen, J. Gillespie, R. Fitch, A. Crespo, K. Sutherlin, B. Poling, S. Tetlak, R. Gilbert, T. Cooper, R. Baranyai, J. W. Pomeroy, M. Kuball, J. J. Maurer, A. Bar-Cohen, *Phys. Status Solidi* **2014**, *11*, 871.
[27] M. N. Touzelbaev, K. E. Goodson, *Diam. Relat. Mater.* **1998**, *7*, 1.
[28] J. W. J. W. Palko, H. Lee, D. D. Agonafer, C. Zhang, K. W. Jung, J. Moss, J. D. Wilbur, J. Tom, M. T. Barako, F. Houshmand, G. Rong, T. Maitra, C. Gorle, Y. Won, D. Rockosi, I. Mykyta, D. Resler, D. Altman, M. Asheghi, J. G. Santiago, K. E. Goodson, *Proc. 2016 IEEE Intersociety Conf. on Thermal and Thermomechanical Phenomena in Electronic Systems (ITherm)*, IEEE, Piscataway, NJ **2016**, pp. 1511–1517.
[29] F. A. L. Dullien, H. Brenner, *Porous Media: Fluid Transport and Pore Structure*, 2nd ed., Academic Press, San Diego, CA **1992**.
[30] A. Bar-Cohen, P. Wang, *J. Heat Transfer* **2012**, *134*, 51017.
[31] A. Bar-Cohen, *Proc. IEEE Int. Conf. on Microwaves, Communications, Antennas and Electronics Systems, (COMCAS)*, IEEE, Piscataway, NJ **2009**, pp. 1–8.
[32] M. V Corbin, M. M. Debenedictis, D. B. James, S. P. Leblanc, L. R. Paradis, *Proc. 11th Annual AIAA/MDA Technology Conf.* AIAA, Reston, VA **2002**, ADM201460.
[33] R. J. Lade, F. Claeyssens, K. N. Rosser, M. N. R. Ashfold, *Appl. Phys. A: Mater. Sci. Process.* **1999**, *69*, S935.
[34] Y. Wang, D. C. Alsmeyer, R. L. McCreery, *Chem. Mater.* **1990**, *2*, 557.
[35] O. D. Velev, A. M. Lenhoff, *Curr. Opin. Colloid Interface Sci.* **2000**, *5*, 56.
[36] M. L. K. Hoa, M. Lu, Y. Zhang, *Adv. Colloid Interface Sci.* **2006**, *121*, 9.
[37] P. V Braun, P. Wiltzius, *Nature* **1999**, *402*, 603.
[38] X. Yu, Y. J. Lee, R. Furstenberg, J. O. White, P. V. Braun, *Adv. Mater.* **2007**, *19*, 1689.
[39] Y. V. Naidich, V. P. Umanskii, I. A. Lavrinenko, *Strength of the Diamond–Metal Interface and Brazing of Diamonds*, Cambridge International Science Publishing, Cambridge **2007**.
[40] G. A. Slack, S. F. Bartram, *J. Appl. Phys.* **1975**, *46*, 89.
[41] S. J. Bennett, *J. Phys. D: Appl. Phys.* **1978**, *11*, 777.
[42] J.-S. Song, M. A. Winnik, *Macromolecules* **2005**, *38*, 8300.
[43] C. Zhang, G. Rong, J. W. Palko, T. J. Dusseault, M. Asheghi, J. G. Santiago, K. E. Goodson, *Proc. ASME 2015 Int. Technical Conf. and Exhibition on Packaging and Integration of Electronic and Photonic Microsystems*, ASME, New York, NY **2015**, IPACK2015-48262, pp. V002T06A004.
[44] S. Yu, M. Kaviany, *J. Chem. Phys.* **2014**, *140*, 64303.
[45] K. H. Chu, Y. S. Joung, R. Enright, C. R. Buie, E. N. Wang, *Appl. Phys. Lett.* **2013**, *102*, 151602.
[46] N. Zuckerman, N. Lior, *Adv. Heat Transfer* **2006**, *39*, 565.
[47] E. J. Davis, G. H. Anderson, *AIChE J.* **1966**, *12*, 774.
[48] D. Liu, P. S. Lee, S. V. Garimella, *Int. J. Heat Mass Transfer* **2005**, *48*, 5134.
[49] C. J. Glassbrenner, G. A. Slack, *Phys. Rev.* **1964**, *134*, A1058.
[50] D. D. Agonafer, J. Palko, Y. Won, K. Lopez, T. Dusseault, J. Gires, M. Asheghi, J. G. Santiago, K. E. Goodson, *Proc. 2014 IEEE Compound Semiconductor Integrated Circuit Symp. (CSICS)*, IEEE, Piscataway, NJ **2014**, pp. 1–4.
[51] A. V. Diniz, N. G. Ferreira, E. J. Corat, V. J. Trava-Airoldi, *Diam. Relat. Mater.* **2004**, *13*, 526.
[52] H. W. Coleman, W. G. Steele, *Experimentation, Validation, and Uncertainty Analysis for Engineers*, John Wiley & Sons, Inc., Hoboken, NJ **2009**.

ADVANCED FUNCTIONAL MATERIALS

Supporting Information

for *Adv. Funct. Mater.*, DOI: 10.1002/adfm.201703265

Extreme Two-Phase Cooling from Laser-Etched Diamond and Conformal, Template-Fabricated Microporous Copper

*James W. Palko, Hyoungsoon Lee, Chi Zhang, Tom J. Dusseault, Tanmoy Maitra, Yoonjin Won, Damena D. Agonafer, Jess Moss, Farzad Houshmand, Guoguang Rong, Joshua D. Wilbur, Derrick Rockosi, Ihor Mykyta, Dan Resler, David Altman, Mehdi Asheghi, Juan G. Santiago, and Kenneth E. Goodson**

Supporting Information

Extreme Two-Phase Cooling from Laser-Etched Diamond and Conformal, Template-Fabricated Microporous Copper

James W. Palko,[1,7] Hyoungsoon Lee,[2] Chi Zhang,[1] Tom J. Dusseault,[1] Tanmoy Maitra,[1] Yoonjin Won,[3] Damena D. Agonafer,[4] Jess Moss,[1] Farzad Houshmand,[1] Guoguang Rong,[5] Joshua D. Wilbur,[1] Derrick Rockosi,[6] Ihor Mykyta,[6] Dan Resler,[6] David Altman,[6] Mehdi Asheghi,[1] Juan G. Santiago,[1] Kenneth E. Goodson[1*]

[1)] Department of Mechanical Engineering, Stanford University, Stanford, CA, USA
[2)] School of Mechanical Engineering, Chung-Ang University, Seoul, South Korea
[3)] Department of Mechanical and Aerospace Engineering, University of California, Irvine, CA USA
[4)] Department of Mechanical Engineering and Materials Science, Washington University, St. Louis, MO, USA
[5)] Electronics and Communication Engineering Department, Suzhou Vocational Institute of Industrial Technology, Suzhou, China
[6)] Advanced Technology Programs, Raytheon Integrated Defense Systems, Sudbury, MA, USA
[7)] Department of Mechanical Engineering, University of California, Merced, CA, USA

*- corresponding author, email: goodson@stanford.edu

Simulations of extended surface efficiency for diamond and silicon

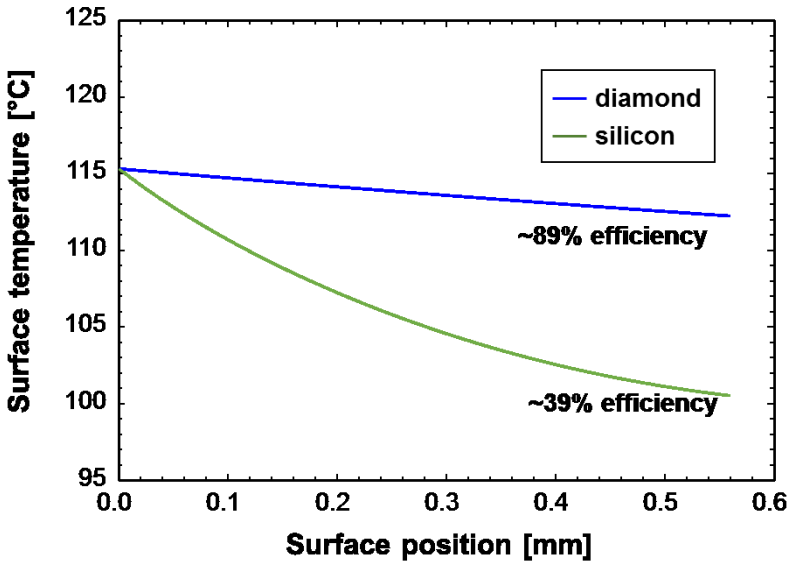

Supplementary Figure 1: Surface temperature for triangular fins with 0.5 mm base and 0.5 mm height, simulated for diamond and silicon with surface $h = 10^6$ W m^{-2} K^{-1}.

Supplementary Figure 1 shows the surface temperature simulated (as described in the Experimental Section) for triangular fins with 0.5 mm base and 0.5 mm height composed of diamond (k = 1800 W m^{-1} K^{-1}) and silicon (k = 150 W m^{-1} K^{-1}) with surface $h = 10^6$ W m^{-2} K^{-1} and a fluid ambient temperature of 100 ^{o}C. The relatively low thermal conductivity of silicon leads to high conduction resistance through the fin and a rapid drop in surface temperature, whereas diamond maintains a far more uniform surface temperature. As a result, the diamond

fin is highly efficient, dissipating ~89% of the heat of a surface of equal size at uniform temperature, whereas the silicon fin has an efficiency of only ~39%.

Surface roughness of laser ablated CVD diamond and electrodeposited copper inverse opal

We characterized the surface roughness of CVD diamond following laser ablation and graphitic carbon removal via profilometery. Supplementary Figure 2 shows three surface profiles of a laser ablated CVD diamond channel sidewall measured from the bottom of the channel to the top at different positions along the channel axis using a stylus with tip radius of 12.5 µm.. A fragment was broken from the larger die to expose the sidewall for scanning. The profiles in Supplementary Figure 2 are referenced to a cubic polynomial baseline fitted to the raw positions to eliminate larger scale topography of the channel. The resulting root mean square (RMS) roughness is 3.4 µm.

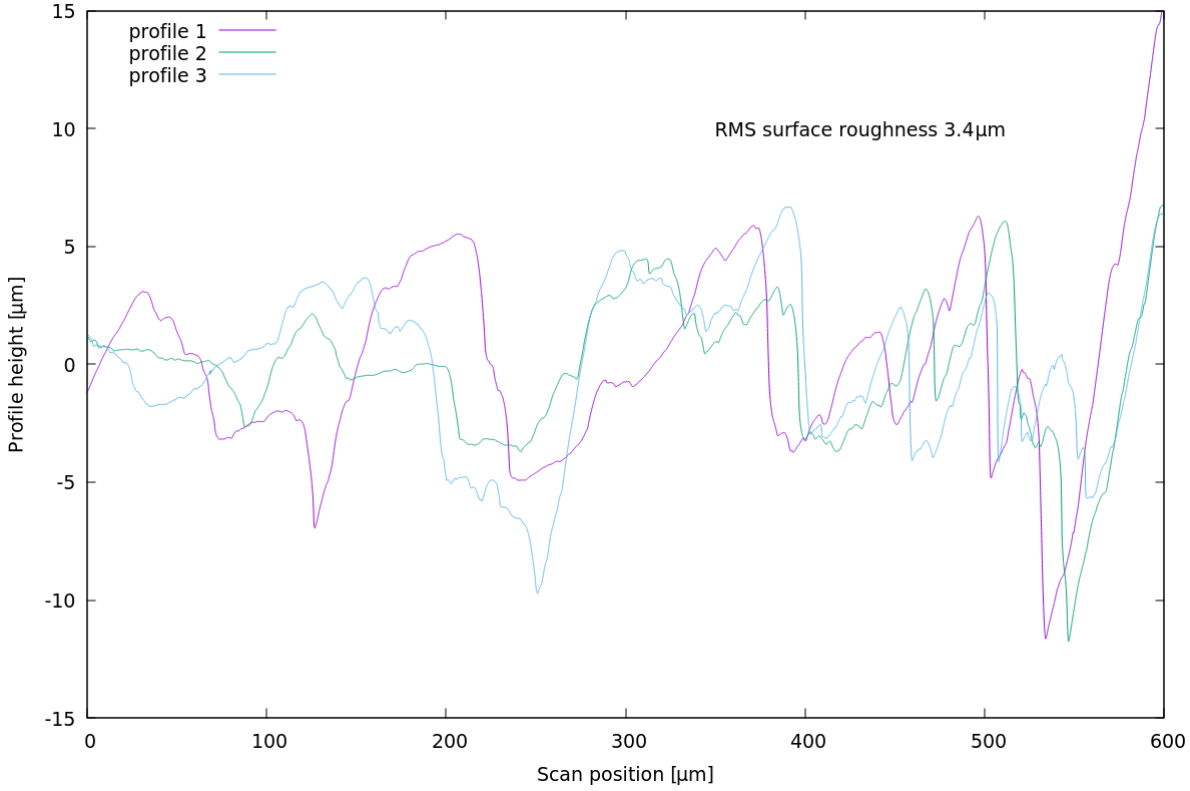

Supplementary Figure 2: Surface roughness of a representative channel sidewall in CVD diamond produced by laser ablation and following graphitic carbon removal. Roughness features are shown relative to a cubic polynomial baseline fit to the raw surface positions. The three profiles are taken at different positions along the channel axis, with the scan direction of each profile from channel bottom to top. RMS roughness is 3.4 µm.

We also measured, via profilometery, the surface roughness of a representative copper inverse opal (CIO) sample from the study with pore size of 5 µm deposited on a planar silicon substrate (Supplementary Figure 3). RMS roughness of the CIO is 0.6 µm.

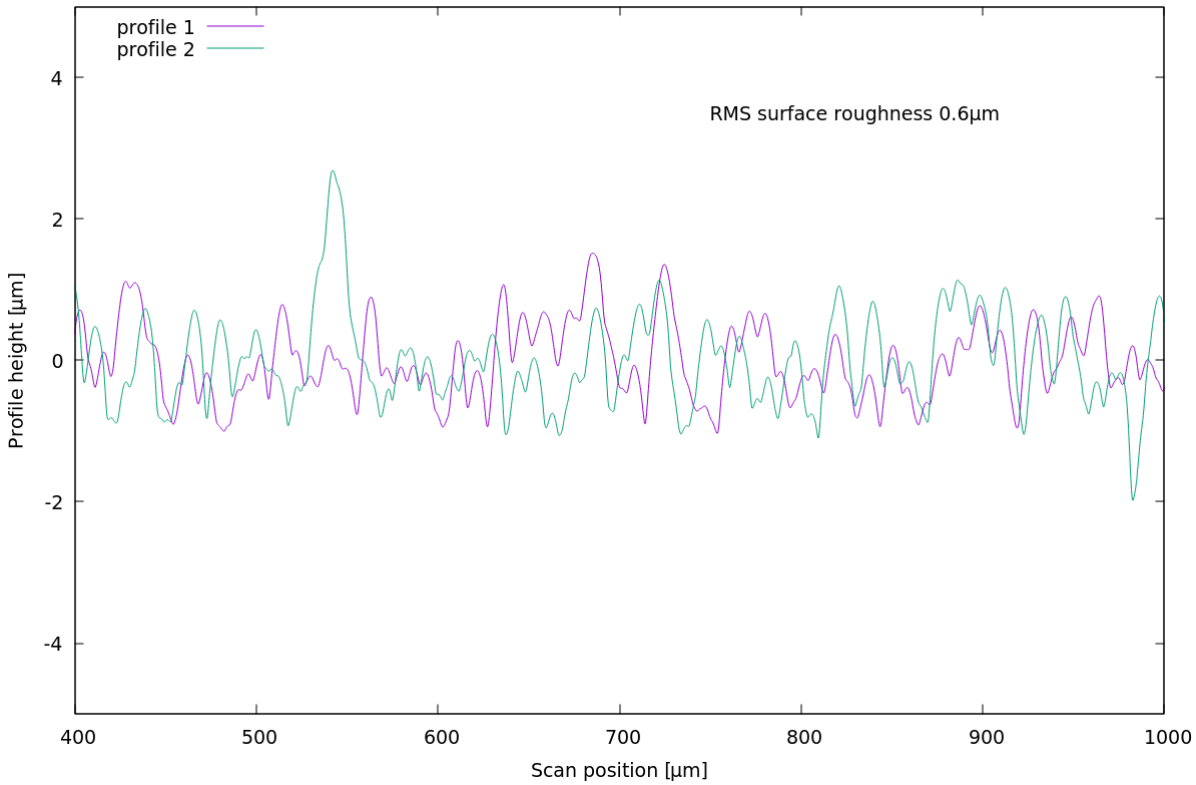

Supplementary Figure 3: Surface roughness of a representative CIO sample from the study grown on planar substrate. Roughness features are shown relative to a quadratic polynomial baseline fit to the raw surface positions. RMS roughness is 0.6 µm.

Microfluidic manifold design and construction

Liquid supply and vapor extraction from the extended surfaces of the diamond/porous copper heat sink requires microfluidic routing to maintain short transport distances of both phases and minimize corresponding pressure drops. Supplementary Figure 4 shows the construction of the manifold used to route liquid to the heat spreader surface and allow vapor escape from it. The manifold is fabricated through layering sheets of polyimide that together form a three dimensional system of liquid and vapor paths.

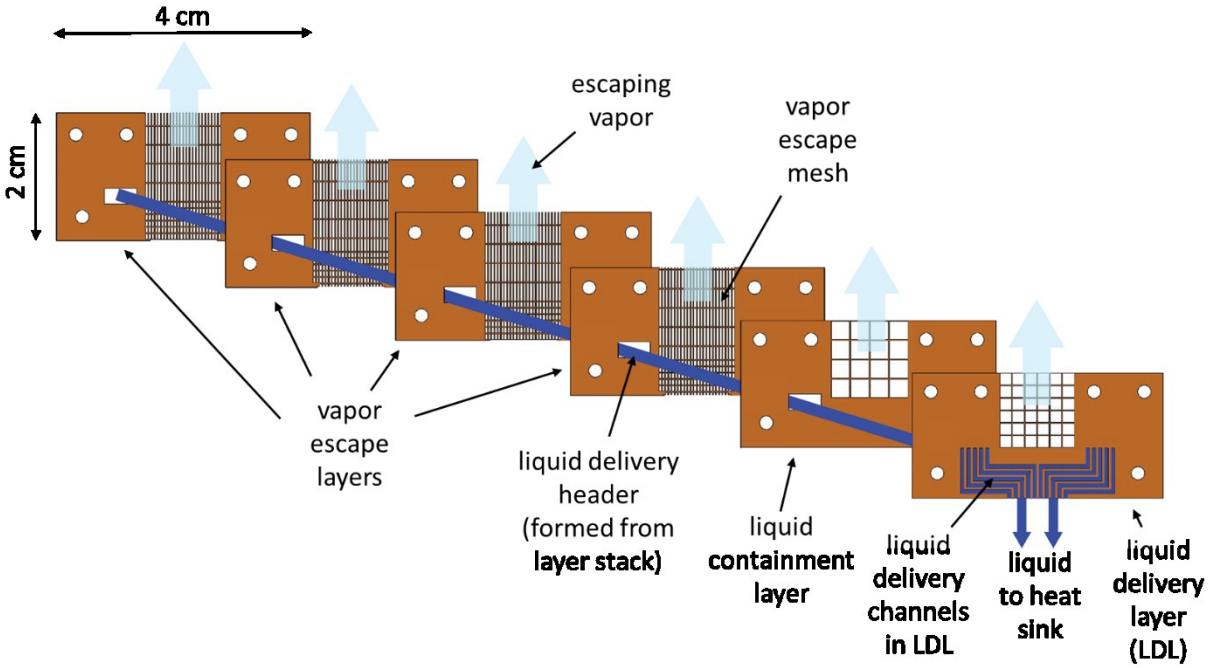

Supplementary Figure 4: Exploded view of a portion of the layered polyimide microfluidic manifold assembly. This portion corresponds to a single channel in the diamond heat spreader.

Three types of layers comprise the manifold:

1. Liquid delivery layer (LDL): This layer transports liquid water to the heat spreader surface. Water enters the channels of the LDL from a direction normal to the layer (through channels formed by overlapping openings in all layers) and flows along the channels defined in the layer as seen in Supplementary Figure 4. The thickness of each LDL layer is 50 μm. Liquid is delivered to the bottom of the heat sink channels.
2. Liquid containment layers: Solid walls are present on either side of the LDL channels and retain liquid in the LDL channels. The thickness of each liquid containment layer is 25 μm.
3. Vapor escape layers: The vapor escape layers serve as spacers to ensure alignment of the LDLs at the troughs of the heat sink. The center sections of the vapor escape layers are formed into meshes with overlapping openings that allow vapor to exit from the system. The thickness of each vapor escape layer is 125 μm.

Supplementary Figure 5 shows a cross section of the mated manifold/heat sink system and the paths of liquid water through the LDL and vapor escape through the spacer layers.

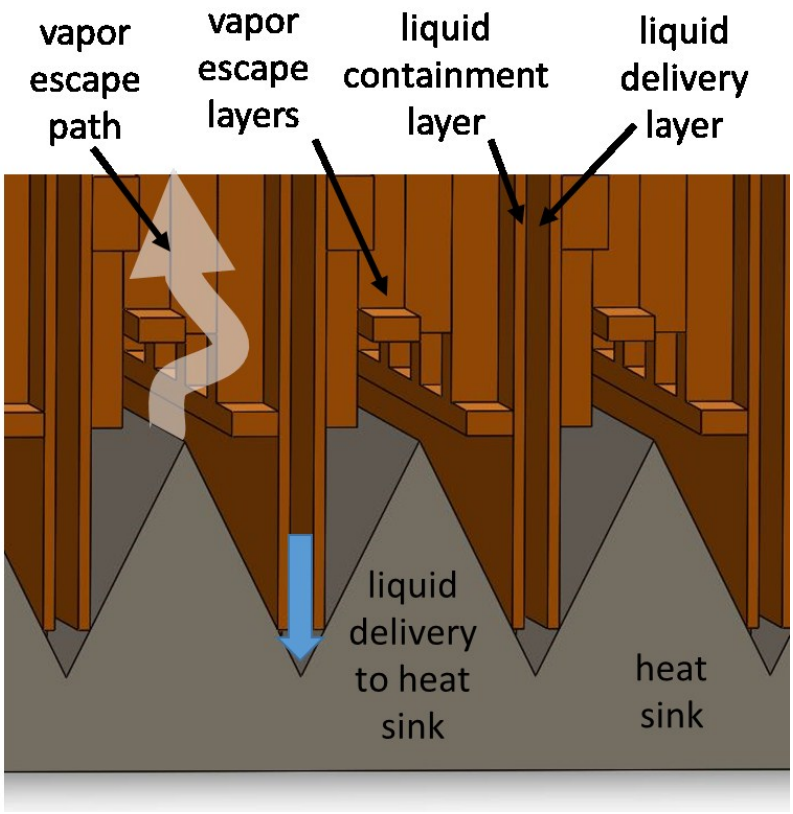

Supplementary Figure 5: Cross section of layered manifold mated to heat sink. The separation between the vapor escape layers and the heat sink has been enlarged for clarity.

The polyimide layers forming the manifold are cut using nanosecond pulsed UV laser ablation. Supplementary Figure 6 shows the assembly of the manifold following layer cutting. The manifold layers are clamped between polycarbonate end plates which provide fluidic connections to the external liquid supply.

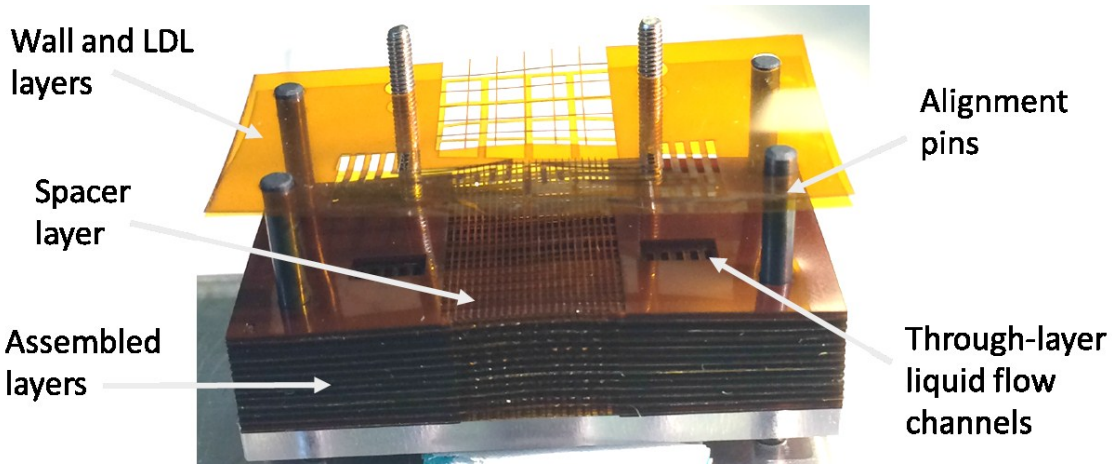

Supplementary Figure 6: Manifold assembly.

Supplementary Figure 7 shows a cross sectional view of the full manifold mated to the heat sink.

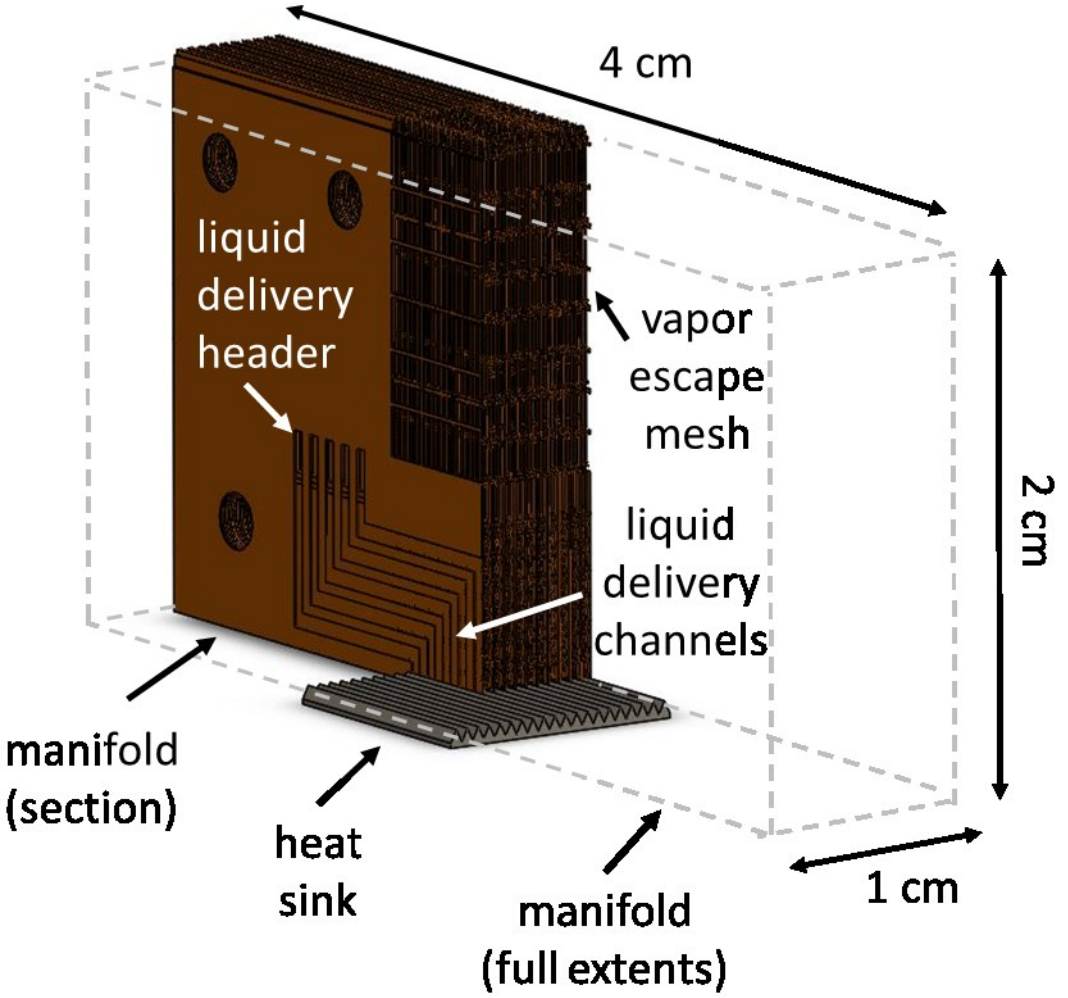

Supplementary Figure 7: Dual cross section of assembled manifold mated to heat sink.

Heat transfer characterization experimental setup

Heat transfer characterization is conducted in an open circuit flow facility, with heat supplied by a thin film platinum heater fabricated on a silicon die mated to the heat sink, as described in the Experimental Section. Supplementary Figure 8 shows a schematic of the facility for boiling experiments.

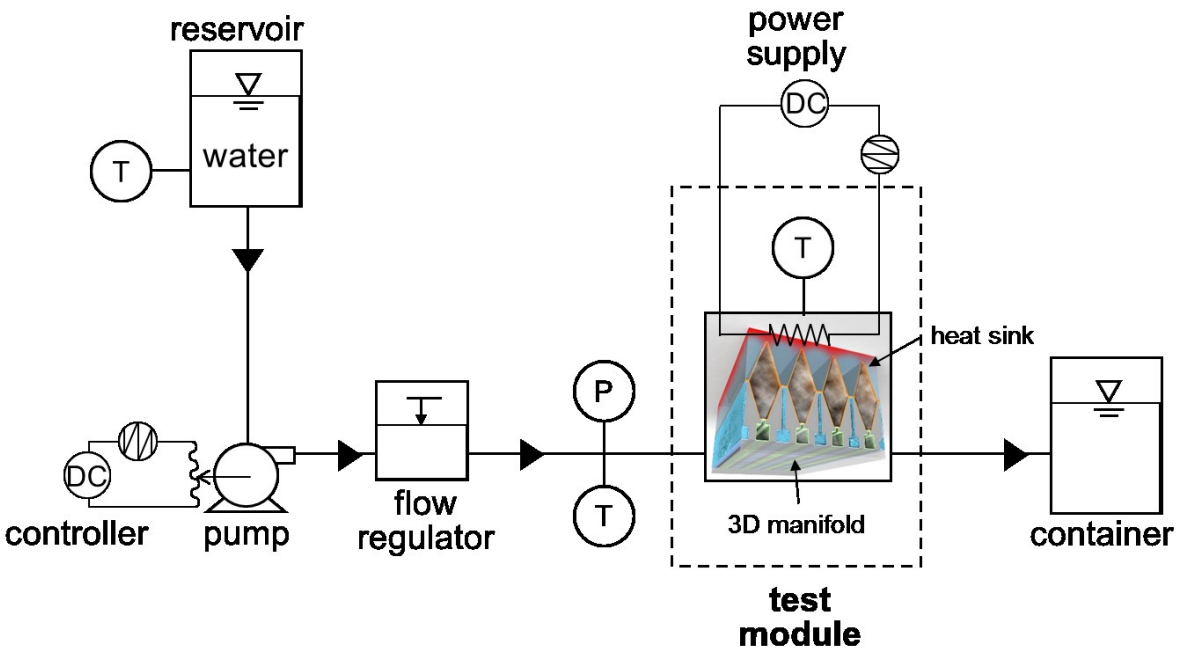

Supplementary Figure 8 Schematic of experimental facility used for heat transfer experiments.

The heat sink is mated to a silicon die with eutectic GaInSn thermal interface material. The heat sink is heated through the die by a thin film platinum heater deposited on the opposite side of the silicon die. Temperature is measured at the center of the heated surface with a k-type thermocouple. Due to the high heat fluxes, a large temperature drop occurs in the silicon die between the heater and heat sink base. In order to accurately determine the temperature at the base of the diamond, temperature drop across the silicon is integrated using the temperature dependent conductivity of silicon.[1] The heated area is 10 mm × 7 mm. Due to the large lateral extent of the heater compared to the thickness of the silicon die (0.525 mm), spreading of heat within the die is small except near the heater edges. Supplementary Figure 9 shows the heating geometry and a simulation of the temperature distribution within the heater die and heat sink with heat flux of 1 kW cm^{-2} at the heater surface and $h = 10^6$ W m^{-2} K^{-1} at the heat sink surface. This simulation was performed with the entire top surface active, but for experiments the manifold only supplies liquid to an area of 10 mm × 8 mm, further reducing any lateral heat spreading.

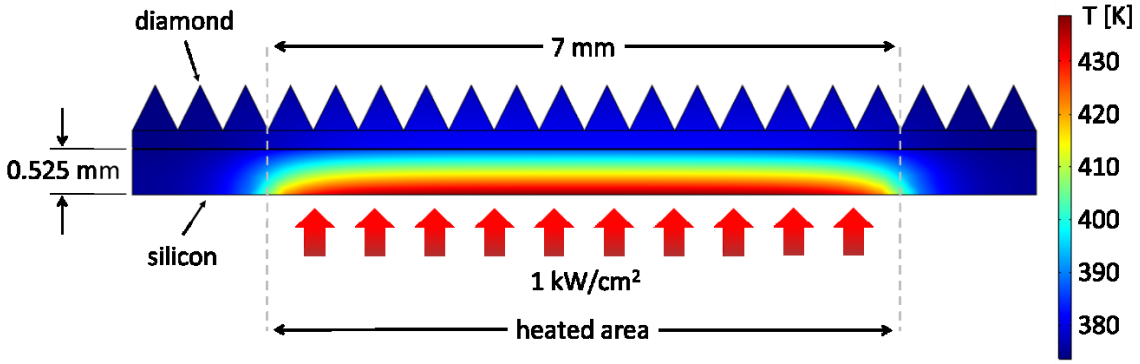

Supplementary Figure 9: Temperature distribution in heater die and heat sink.

References

1. Glassbrenner, C. J. & Slack, G. A. Thermal Conductivity of Silicon and Germanium from 3K to the Melting Point. *Phys. Rev.* **134,** A1058–A1069 (1964).